Engineering Fracture Mechanics 321 (2025) 111130

Contents lists available at ScienceDirect

Engineering Fracture Mechanics

journal homepage: www.elsevier.com/locate/engfracmech

Graphical solutions to bond capacity and bond-slip behavior of pull-off/out joints with various adherents, adhesives, and substrates

Lingzhen Li [a], Eleni Chatzi [b], Christoph Czaderski [c], Elyas Ghafoori [d], Xiao-Ling Zhao [a,*]

[a] Department of Civil and Environmental Engineering, The Hong Kong Polytechnic University, Hong Kong, China
[b] Institute of Structural Engineering (IBK), ETH Zürich 8093 Zürich, Switzerland
[c] Empa, Swiss Federal Laboratories for Materials Science and Technology, Structural Engineering Research Laboratory, 8600 Dübendorf, Switzerland
[d] Institute for Steel Construction, Faculty of Civil Engineering and Geodetic Science, Leibniz University Hannover 30167 Hannover, Germany

A R T I C L E I N F O

Keywords:
Wine Glass Model
Graphical Solution
Analytical Solution
Bond capacity
Bond-Slip Behavior

A B S T R A C T

This study investigates the bond capacity and bond-slip behavior of pull-off (lap-shear) and pull-out joints with various adherents, adhesives, and substrates, filling the research gap in existing models that fail to account for the adherent nonlinear stress–strain behavior. A “Wine Glass model”, offering an elegant graphical and analytical solution to computation of bond capacity, is proposed. This model relies on two key assumptions: (i) a sufficient bond length (longer than an effective bond length) and (ii) a monotonically increasing stress–strain behavior of the adherent. The adherent stress–strain ($\sigma - \varepsilon$) curve and the stress axis (σ-axis) can be visualized as a wine glass. In this analogy, the interfacial fracture energy divided by the adherent thickness (G_f/t) represents the wine poured into the glass. The resulting height of wine corresponds to the adherent tensile stress, with respect to the bond capacity (F_b). The Wine Glass model unveils the mechanism governing bond capacity. Based on the Wine Glass model, an intuitive bond-slip post-processing method, which features a graphical solution as well, is then introduced. The Wine Glass model and associated bond-slip post-processing method are validated on pull-off/out tests corrected from literature, involving linear and nonlinear adherents, linear and nonlinear adhesives, and various substrate materials.

1. Introduction

Modern structures often comprise composite components, including reinforced concrete (RC) structures, fiber reinforced composite (FRP) structures, and metal matrix composites (MMC). These components can be abstracted as reinforcing elements (such as rebars, strips, and fibers) bonded onto/into substrates. Extensive experimental observations, such as Refs. [1–4], highlighted that debonding between adherents and substrates is a typical failure mode. Therefore, understanding bond behavior is essential for ensuring the integrity and longevity of these structures.

* Corresponding author.
E-mail addresses: lingzhen.li@polyu.edu.hk (L. Li), chatzi@ibk.baug.ethz.ch (E. Chatzi), christoph.czaderski@empa.ch (C. Czaderski), ghafoori@stahl.uni-hannover.de (E. Ghafoori), xiao-lin.zhao@polyu.edu.hk (X.-L. Zhao).

https://doi.org/10.1016/j.engfracmech.2025.111130
Received 19 December 2024; Received in revised form 21 February 2025; Accepted 6 April 2025
Available online 10 April 2025

Nomenclature

b	Adherent strip width
D	Adherent rebar diameter
E	Adherent E-modulus
F_b	Bond capacity
G_f	Fracture energy of the bonding interface
$G_{f,i}$	Partial fracture energy at slip s_i
s	Slip of adherent strip
s_i	Slip of adherent strip at x_i
t	Adherent strip thickness
x	Coordinate in the loading direction
x_i	A random location in the bond line
σ	Adherent tensile stress
σ_b	Adherent tensile stress with respect to bond capacity
σ_i	Adherent tensile stress at x_i
ε	Adherent tensile strain
ε_i	Adherent tensile strain at x_i
τ	Shear stress in the bond line

Bond capacity and bond-slip behavior are two fundamental and crucial aspects of bond behavior. Bond capacity refers to the maximum load transferred between the adherent and substrate. Meanwhile, bond-slip behavior, regarded as a "constitutive" interfacial behavior, helps analyze the debonding process. For linear adherents, such as carbon FRP (CFRP), the analyses of bond capacity and bond-slip behavior are straightforward, as the adherent can be characterized by a single E-modulus. Numerous models, such as Equations (1) and (2) and those in Refs. [5-10], have been well-established for bonded systems comprising linear adherents. Solving this second order differential equation employing two boundary conditions, one easily determines the behavior of bonded joints comprising linear adherents.

$$\frac{d^2s}{dx^2} - \frac{\tau}{E \cdot t} = 0 \tag{1}$$

$$F_b = b \cdot \sqrt{2E \cdot t \cdot G_f} \tag{2}$$

where s denotes the adherent slip, as a function of the coordinate of the bonding interface (x); τ, which is a function of s, represents the shear stress at the bonding interface; E, b, and t represent the E-modulus, width, and thickness of the adherent strip, respectively; F_b denotes the bond capacity; G_f stands for the fracture energy of the bonding interface.

On the contrary, for adherents featuring nonlinear stress–strain behavior, such as shape memory alloys (SMAs), Equations (1) and (2) are no longer valid. Analyzing the experimental behavior and establishing associated models present challenges [11–14], given that the adherent stiffness and strength vary with load.

Existing techniques for investigating bond behavior fall into three categories: (i) testing based on short bonding lengths, (ii) testing based on long bonding lengths, and (iii) modelling with varying bonding lengths. The first category focuses on short bonds, which exhibit relatively even interfacial shear stress distributions and reduced bond capacities. The interfacial shear stress/strength is measured by dividing tensile force by bonding area [15-18]. However, these techniques are not suitable for long bonds, which are more practical in engineering applications. The second category largely relies on dense strain measurements of adherents, accommodating long bonds. By analyzing strains at two adjacent points, one can infer the average bond behavior between these two points. External bonds, with exposed adherents, can be easily measured using strain gauges and the digital image correlation (DIC) technique [19–21]. On the other hand, internal bonds, such as steel rebars embedded in concrete, pose measurement challenges; optical fiber measurement provides a solution for assessing these internal bonds [22,23]. The third category employs numerical models, which can address various scenarios (short/long bond lengths, linear/nonlinear adherents, low/high interfacial fracture energy etc.). In this category, assessing bond-slip behavior commonly involves iterative simulations to fit experimentally measured load–displacement curves [11,14,24], which is time-consuming for engineering applications. Despite their versatility, these techniques either require specific measurement efforts or face certain limitations in practical applications. It is worth noting the analytical modelling of adhesive bondline in composite girders [25,26] and lap-shear joints [27] also included the nonlinear material characteristics of flexible adhesive. However, a general and comprehensive analytical model for bond capacity that accommodates both linear and nonlinear adherents is still lacking.

This study proposes a "Wine Glass model", offering an elegant graphical and analytical solution, to accurately estimate bond capacities of various bonded joints in shear. It addresses challenges arising from the nonlinear stress–strain behavior of adherents. Based on the Wine Glass model, an intuitive bond-slip post-processing model, which features a graphical solution as well, is then proposed. These two models accommodate pull-off (lap-shear) and pull-out configurations, linear and nonlinear adherents, linear and nonlinear adhesives, and various substrates materials. This paper is an extension of a conference paper [28].

2. Analytical model setup

Fig. 1(a) and (b) depict a general lap-shear (pull-off) joint and a general pull-out joint, respectively. In both cases, the bond lengths are assumed to be sufficiently long, ensuring that the loads acting on the right ends do not induce shear deformation at the left (free) ends. There is a threshold bond length, known as the effective bond length, beyond which the bond capacity does not increase. Practically, a bond length longer than an effective bond length can be considered sufficiently long. An additional assumption is that the stress–strain behavior of the adherent monotonically increases. It aligns with the behavior of the majority of engineering materials and allows for a later representation of the supplementary strain energy. Fig. 1(c) and (d) schematically illustrate an infinitesimal element of adherent strip and an infinitesimal element of rebar, respectively. For brevity, the model derivation is based on lap-shear joints, and it can be easily extended to involve pull-out joints. Lap-shear joints are also known as pull-off joints; they are interchangeably used in the current study.

For lap-shear joints, the equilibrium of an adherent strip can be expressed as Equation (3).

$$\frac{d\sigma}{dx} = \frac{\tau}{t} \tag{3}$$

where σ and τ represent the tensile and shear stresses, respectively, applied on the adherent infinitesimal element; t denotes the adherent strip thickness, while x refers to the coordinate in the longitudinal (loading) direction. For pull-out joints, t in Equation (3) and following derivation should be replaced by $D/4$, where D is the rebar diameter.

In the current model derivation, the substrate deformation is ignored due to the more pronounced deformation of the adherent strip. Consequently, the engineering strain of the adherent strip is computed via Equation (4). By multiplying Equations (3) and (4), one obtains Equation (5).

$$\varepsilon = \frac{ds}{dx} \tag{4}$$

$$\varepsilon \cdot \frac{d\sigma}{dx} = \frac{\tau}{t} \cdot \frac{ds}{dx} \tag{5}$$

where s denotes the relative displacement (slip) between the adherent strip and substrate, while ε represents the tensile strain of the adherent strip.

An integral of Equation (5) from the free end ($x = 0$) to an arbitrary position ($x = x_i$) along the bond line in Fig. 1(a) is expressed as Equation (6). Given the assumption of the sufficient bond length, the slip at the free end is zero, i.e., $s|_{x=0} = 0$. In the meantime, the tensile stress is zero there, i.e., $\sigma|_{x=0} = 0$, due to the free surface. Therefore, by replacing the integration variable in Equation (6) from x to σ on the left-hand side and from x to s on the right-hand side, one obtains Equation (7).

$$\int_0^{x_i} \varepsilon \cdot \frac{d\sigma}{dx} dx = \int_0^{x_i} \frac{\tau}{t} \cdot \frac{ds}{dx} dx \tag{6}$$

$$\int_0^{\sigma_i} \varepsilon d\sigma = \int_0^{s_i} \frac{\tau}{t} ds \tag{7}$$

Hereinafter, the model derivation does not rely on the Euclidean space (e.g., the aforementioned x coordinate). On the contrary, the analysis remains in the stress–strain ($\sigma - \varepsilon$) space and bond-slip ($\tau - s$) space. This feature distinguishes the current model from many existing models.

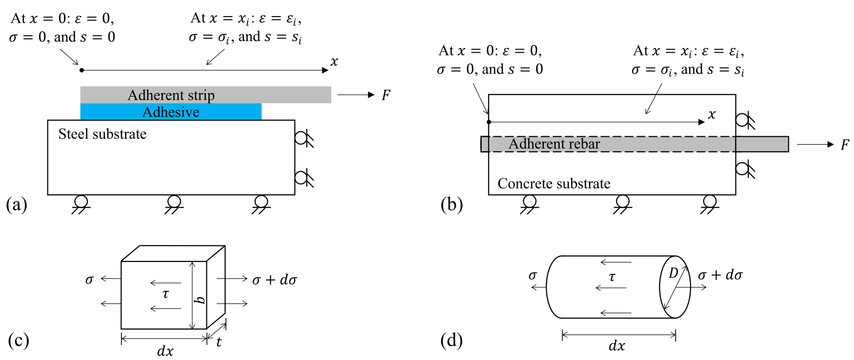

Fig. 1. Schematics of (a) a lap-shear (pull-off) joint, (b) a pull-out joint, (c) an infinitesimal element of adherent strip, and (d) an infinitesimal element of adherent rebar.

In the context of a monotonically increasing stress–strain curve, the left-hand side of Equation (7) represents the adherent supplementary strain energy, as shown in Fig. 2 (a). The right-hand side of Equation (7) can be replaced by $G_{f,i}/t$, where $G_{f,i}$ is the partial fracture energy expressed in Equation (8) and illustrated in Fig. 2 (b).

$$G_{f,i} = \int_0^{s_i} \tau ds \tag{8}$$

$G_{f,i}$ refers to a part of the (total) fracture energy when the slip (s_i) is less than the ultimate slip. When a random location in the bond line (x_i in Fig. 1 (a)) experiences complete damage, the fracture energy at this point is fully dissipated. As a result, $G_{f,i}$ represents the (total) fracture energy, while the tensile stress held in the adherent strip (σ_i) corresponds to the bond capacity.

Substituting Equation (8) into Equation (7) leads to Equation (9), which serves as a governing equation of lap-shear joints. This governing equation links the fracture behavior at the bonding interface and the stress–strain behavior of the adherent strip. It leads to an elegant graphical solution to bond capacity (in Section 3) and an intuitive graphical solution to a post-processing method for bond-slip behavior (in Section 4). Replacing t by $D/4$, the governing equation serves for pull-out joints as well.

$$G_{f,i} = t \cdot \int_0^{\sigma_i} \varepsilon d\sigma \tag{9}$$

3. Bond capacity

3.1. Graphical interpretation of bond capacity

When the interfacial fracture energy at the loaded end is fully dissipated, Equation (9) turns into Equation (10), which allows for a graphical interpretation of the bond capacity (F_b).

$$\frac{G_f}{t} = \int_0^{\sigma_b} \varepsilon d\sigma \tag{10}$$

$$F_b = \sigma_b \cdot A \tag{11}$$

where σ_b represents the adherent tensile stress with respect to the bond capacity; A denotes the cross-sectional area of adherent strip/rebar.

The left-hand side of Equation (10) represents the interfacial fracture energy divided by the adherent strip thickness (dimensioned fracture energy), while the right-hand side refers to the adherent supplementary strain energy, truncated by the tensile stress level with respect to the bond capacity. Fig. 3 presents a graphical interpretation of Equation (10), where the stress–strain ($\sigma - \varepsilon$) curve of the adherent resembles a wine glass when plotted against the vertical axis (σ-axis). In this analogy, the dimensioned fracture energy (G_f/t) represents the wine in the glass. The height of wine represents the adherent tensile stress at bond capacity. Therefore, this model is referred to as the “Wine Glass model”. Section 3.2 demonstrates the accuracy and robustness of the Wine Glass model in predicting bond capacity, while Section 3.3 exemplifies several representative cases of bond capacity estimation. It is worth nothing that Equation (10) indicates an independence of the proposed Wine Glass model on the specific shape of the bond-slip behavior. Consequently, the bond capacity depends solely on the adherent dimension and stress–strain behavior, as well as the interfacial fracture energy. Depending on cultural background, this model may also be referred to as the “Reservoir model”, “Tea Cup model”, “Smoothie Cup model”, or “Soup Bowl model”.

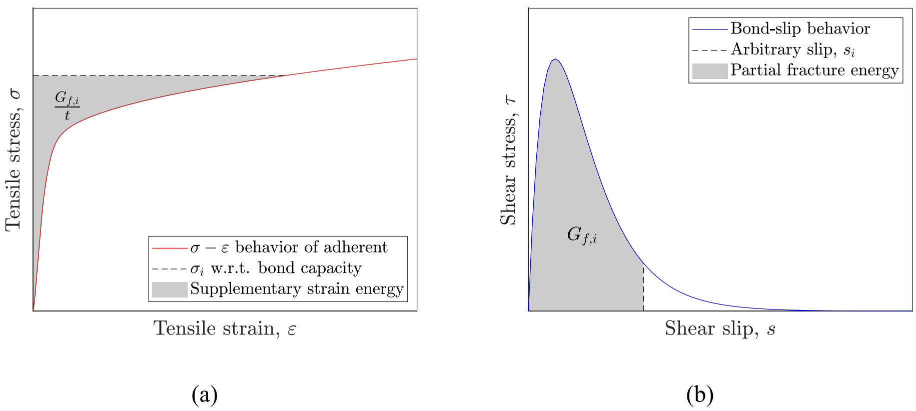

Fig. 2. The relationship between the adherent supplementary strain energy and the adhesive fracture energy. (a) A general nonlinear stress–strain curve and its supplementary strain energy. (b) A schematic bond-slip curve, where the underneath area is the fracture energy (G_f), while the area truncated by a slip (s_i) is the partial fracture energy ($G_{f,i}$).

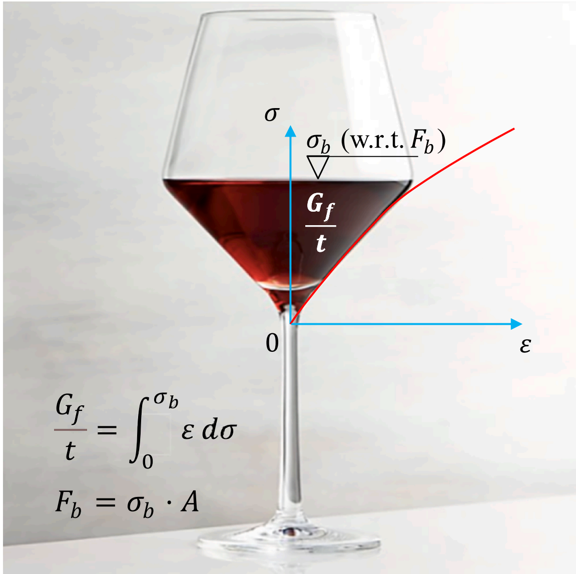

Fig. 3. The Wine Glass model, with the background wine glass adopted from Crate & Barrel [29].

3.2. Validation of the Wine Glass model on general bonded joints in shear

To validate the proposed Wine Glass model, a total of 95 experimental pull-off/out joints were collected from literature, including iron-based SMA (Fe-SMA)-to-steel lap-shear joints [12,13,20,30,31], Fe-SMA-to-concrete lap-shear joints [32], CFRP-to-steel lap-shear joints [19,33,34], CFRP-to-concrete lap-shear joints [21,35], mild-steel-to-steel lap-shear joints [33], Fe-SMA-to-concrete pull-out joints [14], stainless-steel-to-concrete pull-out joints [36], NiTi-SMA-to-CFRP pull-out joints [11], and CFRP-to-concrete pull-out joints [37]. These bonded joints contain (i) pull-off and pull-out configurations, (ii) linear and nonlinear adherents, (iii) linear and nonlinear adhesives, and (iv) various substrate materials (steel, concrete, and composites). Their bond lengths are typically greater than their effective bond lengths, justifying the basic assumption of a sufficient bond length. In existing studies, linear adhesives generally exhibit quasi-linear stress–strain behavior with low fracture energy, typically characterized by triangular bond-slip curves [5,19,38,39]. Conversely, nonlinear adhesives exhibit pronounced nonlinear stress–strain behavior with significantly higher fracture energy, often presented by trapezoidal bond-slip patterns [8,19,38,39]. The proposed Wine Glass model depends solely on the fracture energy, regardless of the bond-slip shape.

The joint geometry (including strip thickness, t, or rebar diameter, D), bonding fracture energy (G_f), and adherent stress–strain

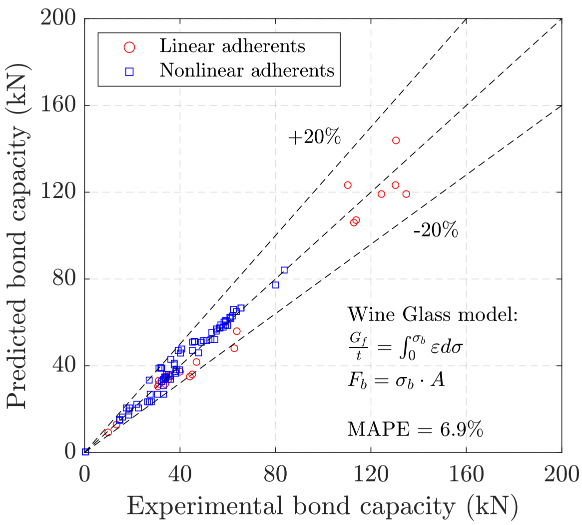

Fig. 4. Bond capacities, Wine Glass model predictions vs. experimental measurements.

($\sigma - \varepsilon$) behavior of 95 bonded joints are reported in literature. By substituting these values into the Wine Glass model, i.e., Equations (10) and (11), one can easily estimate the bond capacities of these 95 bonded joints. Detailed experimental data vs. Wine Glass model prediction is provided in Appendix A. Fig. 4 compares the estimated bond capacities of the 95 bonded joints with their experimentally measured bond capacities reported in literature. The mean absolute percentage error (MAPE) of approximately 7 % confirms the accuracy and robustness of the Wine Glass model in predicting bond capacity of general bonded joints in shear. Alternatively, Equations (10) and (11) and Fig. 3 can be used to determine the interfacial fracture energy with a known bond capacity.

To further demonstrate the accuracy and merits of the proposed Wine Glass model, especially for bonded joints with nonlinear adherents, the well-known Equation (2) is used to compute bond capacities of the 95 bonded joints. Fig. 5 illustrates the bond capacities analyzed using Equation (2) versus the experimental measurements. Two groups can be identified: (i) the proper-estimation group marked with a green background, where model analyses closely align with experimental measurements, and (ii) the overestimation group marked with a red background, where model analyses significantly exceed experimental measurements. In the proper-estimation group, the adherents either exhibit linear stress–strain behavior or only the quasi-linear stage of the nonlinear stress–strain behavior is utilized, making Equation (2) valid. In the overestimation group, adherents display pronounced nonlinear stress–strain behavior, leading to significant overestimation of bond capacities through Equation (2). Incorporating the Wine Glass model, Fig. 6 intuitively explains why the well-known Equation (2) persistently overestimates bond capacities for joints with nonlinear adherents. Additionally, the Wine Glass model reveals that at large adherent strains, varying the bonding fracture energy does not significantly affect the bond capacity.

3.3. Application cases of the Wine Glass model

This section exemplifies bond capacity estimation employing the proposed Wine Glass model, including mild steel lap-shear joints, Fe-SMA lap-shear joints, and CFRP lap-shear joints.

3.3.1. Experiment overview

Fig. 7(a) schematically shows the dimensions of lap-shear joints tested by Li et al. [12,33]. All adherent strips (mild steel, Fe-SMA, and CFRP strips) are 600 mm long, 50 mm wide, with a bond length of 300 mm. Mild steel strips have a thickness of 1.5 mm, an E-modulus of 200 GPa, a yield strength of 400 MPa, a tensile strength of 450 MPa, and an elongation at break of 30 %. CFRP strips have a thickness of 1.4 mm, an E-modulus of 156 GPa, and a nominal tensile strength of 2800 MPa. Non-prestrained and prestrained Fe-SMA strips are 1.5 mm thick, with chord moduli of 153.3 GPa and 137.5 GPa, respectively, measured between 20 and 300 MPa. Their tensile strengths are 1023 MPa and 1022 MPa, respectively, with elongations at break of 53 % and 50 %. Indeed, non-prestrained and prestrained Fe-SMAs are the same material. A prestraining procedure converts the non-prestrained Fe-SMA into the prestrained Fe-SMA, enabling a self-prestressing property of prestressing by heating. Interested readers are referred to Ref. [40] for details of Fe-SMA materials. Fig. 7 (b) illustrates the stress–strain curves of these adherents. The employed bonding agents are SikaDur 30 (a linear adhesive) and SikaPower 1277 (a nonlinear adhesive), both having a thickness of 0.5 mm; their mode-II (shear mode) fracture energy are 1.2 and 12.5 MPa · mm, respectively.

3.3.2. Mild steel lap-shear joints

To facilitate hand calculations, the stress–strain behavior of the mild steel strip is simplified to three straight lines, which are depicted as solid red lines in Fig. 8 and summarized in Table 1. Incorporating the Wine Glass model and the simplified stress–strain

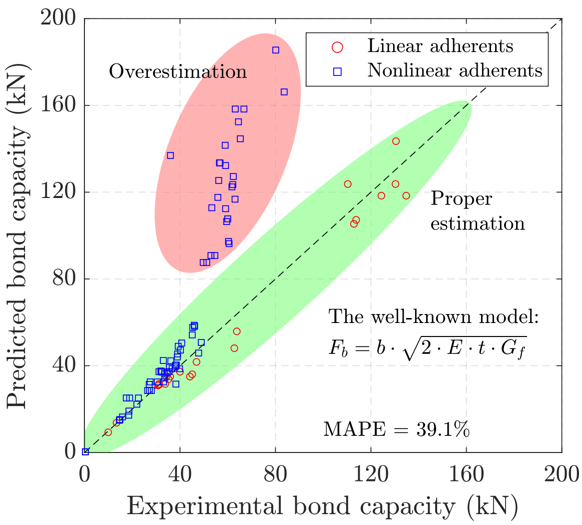

Fig. 5. Bond capacities, predictions using the well-known model vs. experimental measurements.

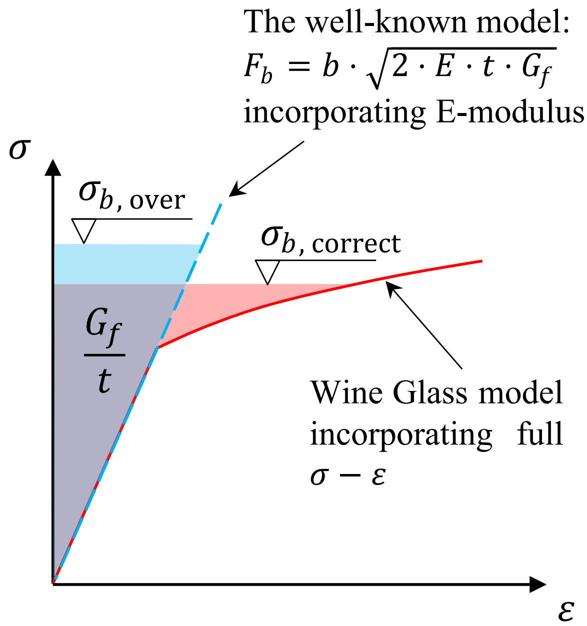

Fig. 6. Demonstration of the well-known model overestimating bond capacities of bonded joints with nonlinear adherents. $\sigma_{b,\text{correct}}$ denotes the correct bond capacity, while $\sigma_{b,\text{over}}$ represents the overestimated bond capacity.

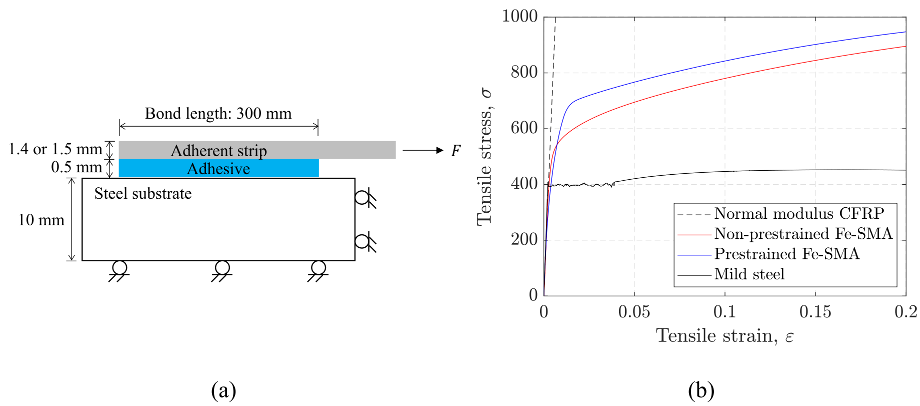

Fig. 7. Schematic view of lap-shear joints with various adherents. (a) Dimensions of lap-shear joints (adherent strips are 50 mm in width). (b) Stress–strain curves of adherent strips.

behavior, three distinct categories are identified in Fig. 8(b) and listed in Table 2; their boundaries are determined using the Wine Glass model, as shown in Equations (12) and (13). (i) If $G_f \leq 0.6$ MPa · mm, the wine glass has a narrow shape, and the mild steel strip remains in the linear elastic stage at the bond capacity. (ii) If $0.6 < G_f < 5.7$ MPa · mm, the mild steel strip yields and strain hardens, and the wine glass displays a narrow base broadening to a wide top; debonding occurs during the strain hardening of the mild steel strip. (iii) If $G_f \geq 5.7$ MPa · mm, the wine overflows from the wine glass, and the tensile loading capacity of the mild steel strip is smaller than the bond capacity; thus, instead of a complete debonding, rupture of the mild steel strip occurs.

$$G_{f,1} = t \cdot \int_0^{\sigma_i} \varepsilon d\sigma = 1.5\text{mm} \cdot \frac{400\text{MPa} \cdot 0.2\%}{2} = 0.6\text{MPa} \cdot \text{mm} \tag{12}$$

$$G_{f,2} = t \cdot \int_0^{\sigma_i} \varepsilon d\sigma = 0.6\text{MPa} \cdot \text{mm} + 1.5\text{mm} \cdot \frac{(450 - 400)\text{MPa} \cdot (3.5 + 10)\%}{2} \approx 5.7\text{MPa} \cdot \text{mm} \tag{13}$$

For the mild steel lap-shear joint comprising a linear adhesive, which possesses a fracture energy of 1.2 MPa · mm, it falls into category (ii). The bond capacity of approximately 31 kN is estimated using Equations (14) and (15), which is close to the experimental measurement of 33 kN.

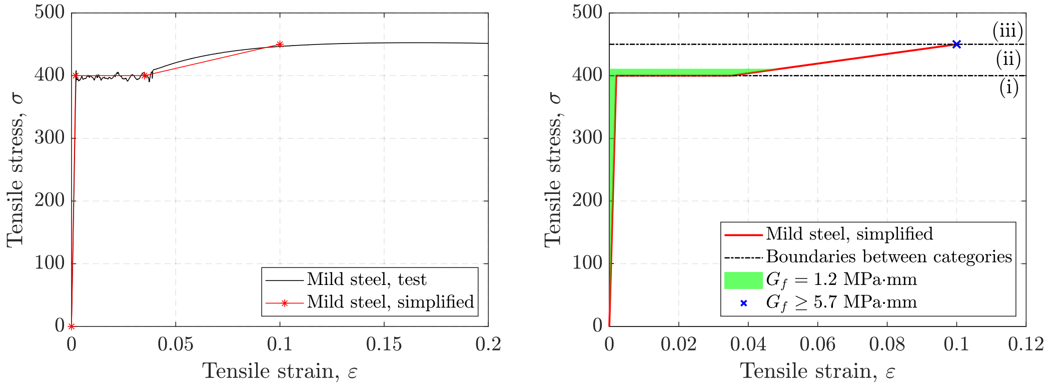

(a) (b)

Fig. 8. Bond capacity of the mild steel joint with a linear adhesive. (a) Stress–strain behavior of the mild steel strip (tensile strain demonstrated up to 20 %). (b) Bond capacity analysis using the Wine Glass model (tensile strain demonstrated up to 12 %).

Table 1
Simplified stress–strain behavior of the mild steel.

Strain (%)	0	0.2	3.5	10
Stress (MPa)	0	400	400	450

Table 2
Categories of bond capacity computation in mild steel bonded joints.

Categories	(i)	(ii)	(iii)
G_f range (MPa · mm)	[0, 0.6]	(0.6, 5.7]	(5.7, $+\infty$)
σ_b range (MPa)	[0, 400]	(400, 450]	Rupture of mild steel strip

$$\sigma_b \approx 400\text{MPa} + \frac{(1.2 - 0.6)\,\text{MPa}\cdot\text{mm}}{1.5\text{mm}\cdot 3.5\%} = 411\text{MPa} \tag{14}$$

$$F_b = 411\text{MPa}\cdot 50\text{mm}\cdot 1.5\,\text{mm} \approx 31\,\text{kN} \tag{15}$$

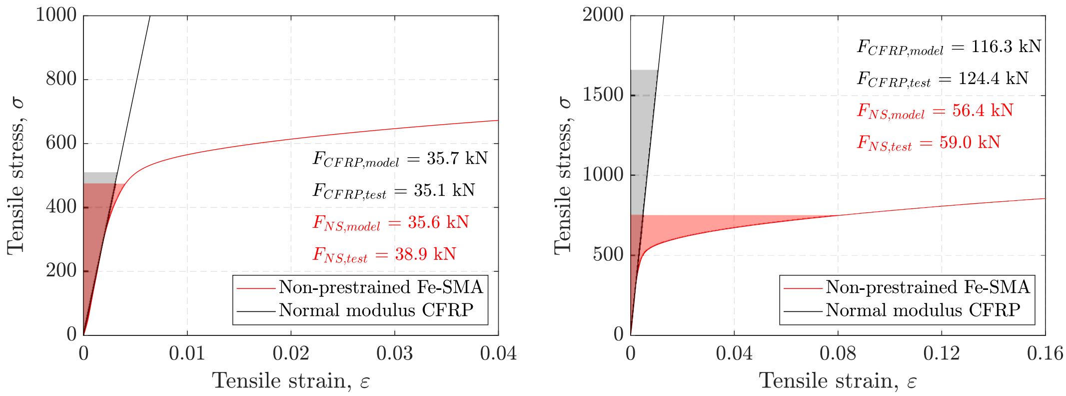

(a) Bonded by a linear adhesive (tensile stress demonstrated up to 1000 MPa).

(b) Bonded by a nonlinear adhesive (tensile stress demonstrated up to 2000 MPa).

Fig. 9. Bond capacities of non-prestrained Fe-SMA and CFRP joints. The footnotes “NS” and “CFRP” represent non-prestrained Fe-SMA and CFRP, respectively.

For the joint consists of a nonlinear adhesive, which possesses a fracture energy of 12.5 MPa · mm, it falls into category (iii); the maximum tensile load of 450 MPa (ultimate tensile strength) × 1.5 mm × 50 mm ≈ 34 kN, which corresponds to the mild steel strip rupture, closely aligns with the experimental measurement of 36 kN.

3.3.3. Fe-SMA vs. CFRP lap-shear joints

Li et al. [12] delivered an experimental study and reported: (i) when bonded by the same linear adhesive, the CFRP and Fe-SMA lap-shear joints exhibit nearly identical bond capacities; (ii) when bonded by the same nonlinear adhesive, the CFRP joint achieves approximately twice the bond capacity of the Fe-SMA joint. Notably, Fe-SMA refers to the non-prestrained Fe-SMA, whose chord modulus (153.3 GPa) is nearly identical to the E-modulus of CFRP (156 GPa). The Wine Glass model can intuitively explain these phenomena.

The fracture energy of the linear adhesive is insufficient to induce a pronounced nonlinear behaviour of the Fe-SMA strip. Consequently, both the CFRP wine glass (the black curve in Fig. 9 (a)) and Fe-SMA wine glass (the red curve in Fig. 9(a)) share similar profiles, resulting in comparable tensile stress levels (height of the wine). Given their similar strip dimensions, the bond capacities of both CFRP and Fe-SMA joints are nearly identical.

When a nonlinear adhesive is used as the bonding agent, the Fe-SMA strip exhibits pronounced nonlinear behavior. As a result, noticeable differences exist between CFRP and Fe-SMA joints. The Fe-SMA wine glass (the red curve in Figure Fig. 9(b)) is wider and shallower compared with the CFRP wine glass (the black curve in Figure Fig. 9(b)). Consequently, the CFRP joint exhibits a bond capacity that is approximately twice as much as that of the Fe-SMA joint. On the other hand, the Fe-SMA joint demonstrates greater tensile strain compared against the CFRP joint, indicating significantly higher ductility for Fe-SMA joints.

3.3.4. Non-prestrained vs. Prestrained Fe-SMA lap-shear joints

Li et al. [12] further reported that (i) with the same linear adhesive, the non-prestrained and prestrained Fe-SMA lap-shear joints exhibit similar bond capacities, while that of the non-prestrained Fe-SMA joint is marginally larger; (ii) with the same nonlinear adhesive, the prestrained Fe-SMA lap-shear joint demonstrates a greater bond capacity. These phenomena can also be visualized by the Wine Glass model.

As previously explained, the insufficient fracture energy of the linear adhesive keeps Fe-SMA strips in the quasi-linear stage of the stress–strain behavior. In this stage, the non-prestrained Fe-SMA wine glass (the red curve in Fig. 10 (a)) is slightly narrower than the prestrained Fe-SMA wine glass (the blue curve in Fig. 10(a)). As a result, the tensile stress level (height of the wine) and the resulting bond capacity of the non-prestrained Fe-SMA joint marginally exceed those of the prestrained Fe-SMA joint.

On the other hand, the nonlinear adhesive, possessing a greater fracture energy, induces pronounced nonlinear behavior of Fe-SMA strips. The prestrained Fe-SMA wine glass (the blue curve in Fig. 10(b)) exhibits a significantly higher profile than the non-prestrained Fe-SMA wine glass (the red curve in Fig. 10(b)). As a result, the tensile stress level (height of the wine) and bond capacity of the prestrained Fe-SMA joint surpass those of the non-prestrained Fe-SMA joint.

3.4. Degrade to solution for linear adherents

When the adherent has a linear stress–strain relationship, such as a CFRP strip, the solution of the bond capacity degrades to the well-known model for CFRP bonded joints (Equation (2)) [5,8]. This is not surprising.

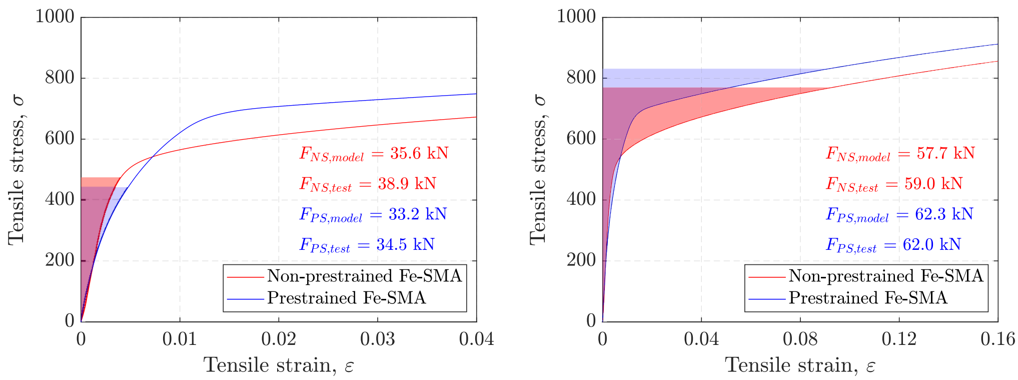

(a) Bonded by a linear adhesive (tensile strain demonstrated up to 4%).

(b) Bonded by a nonlinear adhesive (tensile strain demonstrated up to 16%).

Fig. 10. Bond capacities of non-prestrained and prestrained Fe-SMA joints. The footnotes "NS" and "PS" represent non-prestrained and prestrained Fe-SMAs, respectively.

3.5. Designing failure modes for bonded joints

Incorporating the Wine Glass model, failure modes of bonded joints can be designed, through the choice of adherent dimension and adhesive/mortar for bonding. Fig. 11 depicts two typical nonlinear adherent stress–strain curves (wine glass profiles), which cover a wide range of nonlinear materials: (a) adherents with a yielding plateau and (b) adherents without a yielding plateau.

Table 3 summarizes the three stages in Fig. 11, each assigned with a specific color, and their corresponding failure modes: (i) linear (quasi-linear) stage (marked as red), (ii) nonlinear stage (marked as blue), and (iii) adherent rupture (marked as black). (i) When the dimensioned fracture energy (G_f/t) is within the linear part of the wine glass (the red region), the bonded joint fails due to debonding, with the adherent remaining elastic at joint failure. The well-known Equation (2) remains valid. (ii) When G_f/t exceeds the linear part of the wine glass but remains in the wind glass (the blue region), the bonded joint fails due to debonding, with the adherent staying in the strain-hardening stage at joint failure. Equation (2) is no longer valid. (iii) When G_f/t overflows from the wine glass, the adherent reaches its ultimate strength before fully dissipating the interfacial fracture energy. The bonded joint fails due to adherent rupture, while no debonding occurs; the joint load carrying capacity is independent on the adhesive properties. Analysis in Section 3.3.2 is a realization of this design philosophy. Nevertheless, the tests in Section 3.3.2 were done prior to the development of the Wine Glass model, thus, a design of their failure modes using the Wine Glass model was not possible.

4. Bond-slip behavior

In addition to the bond capacity, assessing the bond-slip behavior is imperative, as it serves as a “constitutive” behavior governing the bonding interface. This section introduces an innovative bond-slip post-processing method based on the Wine Glass model. It relies on the measurement of (i) the adherent stress–strain behavior and (ii) the joint load-slip curve; these measurements are fundamental for nearly every experimental investigation. The solution has a graphical interpretation as well.

A reformulation of Equation (8) leads to Equation (16). Substituting Equation (9) into Equation (16) leads to Equation (17), which is applicable to lap-shear joints. Replacing t in Equation (17) by $D/4$, the bond-slip solution is applicable to pull-out joints as well. Coincidentally, Equation (17) is very similar to an existing bond-slip post-processing method delivered by Biscaia et al. [36].

$$\tau = \frac{dG_{f,i}}{ds} \tag{16}$$

$$\begin{aligned} \tau &= t \cdot \frac{d\left(\int_0^{\sigma_i} \varepsilon d\sigma\right)}{d\sigma} \cdot \frac{d\sigma}{ds} \\ &= t \cdot \varepsilon \cdot \frac{d\sigma}{ds} \\ &= \frac{\varepsilon}{b} \cdot \frac{dF}{ds} \end{aligned} \tag{17}$$

where dF/ds denotes the slope of the load-slip curve; ε represents the adherent tensile strain at the loaded end.

4.1. Graphical interpretation of bond-slip post-processing

Equation (17) suggests that the shear stress in the bond line can be determined by multiplying the slope of the load-slip curve with the adherent tensile strain at the loaded end. Fig. 12 provides a graphical interpretation of the bond-slip post-processing method, whose discrete form is given by Equation (18). Combing a series of ($\tau_{i+1/2}$, $s_{i+1/2}$), one can easily determine the bond-slip behavior.

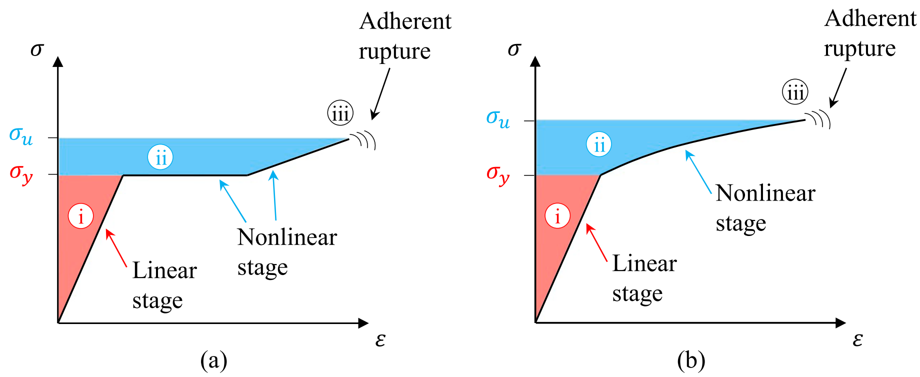

Fig. 11. Distinguishing failure modes using the Wine Glass model: (a) adherent with a yielding plateau, (b) adherent without a yielding plateau. σ_y represents the yielding (or nominal yielding) strength, while σ_u denotes the ultimate tensile strength.

Table 3
States of adherent and bonding interface at joint failure.

	Bonding fracture energy	Adherent	Bonding interface
(i)	$0 < \frac{G_f}{t} \leq \int_0^{\sigma_y} \varepsilon d\sigma$	Elastic stage	Full debonding
(ii)	$\int_0^{\sigma_y} \varepsilon d\sigma < \frac{G_f}{t} < \int_0^{\sigma_u} \varepsilon d\sigma$	Strain-hardening stage	Full debonding
(iii)	$\int_0^{\sigma_u} \varepsilon d\sigma \leq \frac{G_f}{t}$	Rupture	Locally damaged, but no debonding

Notes: σ_y and σ_u represent the yielding strength and ultimate tensile strength, respectively, of nonlinear adherents; G_f denotes the bonding fracture energy; t represents the adherent strip thickness.

During the pull-off/out tests, the tensile loads (F) are typically measured by load cells; the slips (s) can be measured by extensometers or DIC; the adherent strains (ε) at the loaded ends are typically measured by strain gauges or DIC. When the strain measurement at the loaded end is unavailable, the tensile strain can be inferred from the tensile stress (tensile force divided by cross-sectional area) using the stress–strain curve, as depicted in Fig. 12 (a) and (b).

$$\begin{cases} \tau_{i+\frac{1}{2}} = \dfrac{\varepsilon_{i+1/2}}{b} \cdot \dfrac{F_{i+1} - F_i}{s_{i+1} - s_i} \\ \varepsilon_{i+\frac{1}{2}} = \dfrac{\varepsilon_{i+1} + \varepsilon_i}{2} \\ s_{i+\frac{1}{2}} = \dfrac{s_{i+1} + s_i}{2} \end{cases} \tag{18}$$

Built upon the Wine Glass model, this bond-slip post-processing method is tailored for long bonds. During analysis, the focus is exclusively on the loaded end of the pull-off/out joint, while the stress, strain, energy etc., at the middle and free end of the joint are not of concern. This is extremely convenient for pull-out joints where adherents are hidden and difficult to be measured, as it requires minimal experimental measurements and the computation is straightforward. Notably, the tensile force acting on the adherent strip/rebar is balanced by shear stresses distributed over a certain length; this highlights that the bond-slip behavior analyzed through Equations (17) and (18) incorporates contributions from a specific bonding area, rather than being localized solely at the loaded end. In other words, the resulting bond-slip behavior represents an “average” bond-slip behavior over a certain length.

4.2. Application cases of the bond-slip post-processing method

By substituting the joint load-slip curves and adherent stress–strain curves into Equation (17) or (18), one easily infers the bond-slip behavior of a bonded joint. Fig. 13 exemplifies bond-slip behaviors of six representative bonded joints from the 95 collected joints loaded in shear. These six joints involve (i) pull-off and pull-out configurations, (ii) linear and nonlinear adherents, (iii) linear and nonlinear adhesives, and (iv) steel, concrete, and composites as substrates. The close alignment between the bond-slip behaviors analyzed through the current method (solid black curves) and those reported in literature (red dashed curves and dots) confirms the efficacy and wide applicability of the bond-slip post-processing method. The minor differences between the black and red curves/dots do not necessarily reflect errors resulting from the current method, because in literature, bond-slip behaviors are analyzed through certain models as well, rather than direct measurements. Therefore, in addition to existing methods, the current post-processing method offers a simple and robust solution in analyzing bond-slip behaviors.

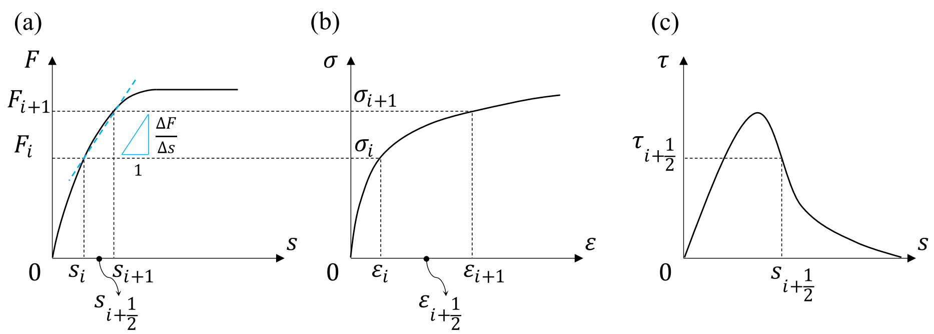

Fig. 12. Graphical interpretation of the bond-slip post-processing method: (a) load-slip curve of the bonded joint, (b) stress–strain curve of the adherent, and (c) inferred bond-slip curve comprising pairs of ($\tau_{i+1/2}$, $s_{i+1/2}$).

4.3. Degrade to solutions for linear adherents

When the adherent features a linear stress–strain behavior, Equation (17) can be extended to two specific forms, namely Equations (19) and (20), each representing a distinct experimental measurement. Equation (19), which is identical to Dai et al. [6], requires a measurement of the adherent tensile strain-slip ($\varepsilon - s$) behavior at the loaded end. Equation (20) relies on a measurement of the tensile load-slip ($F - s$) behavior of the bonded joint.

$$\tau = t \cdot E \cdot \varepsilon \cdot \frac{d\varepsilon}{ds} \tag{19}$$

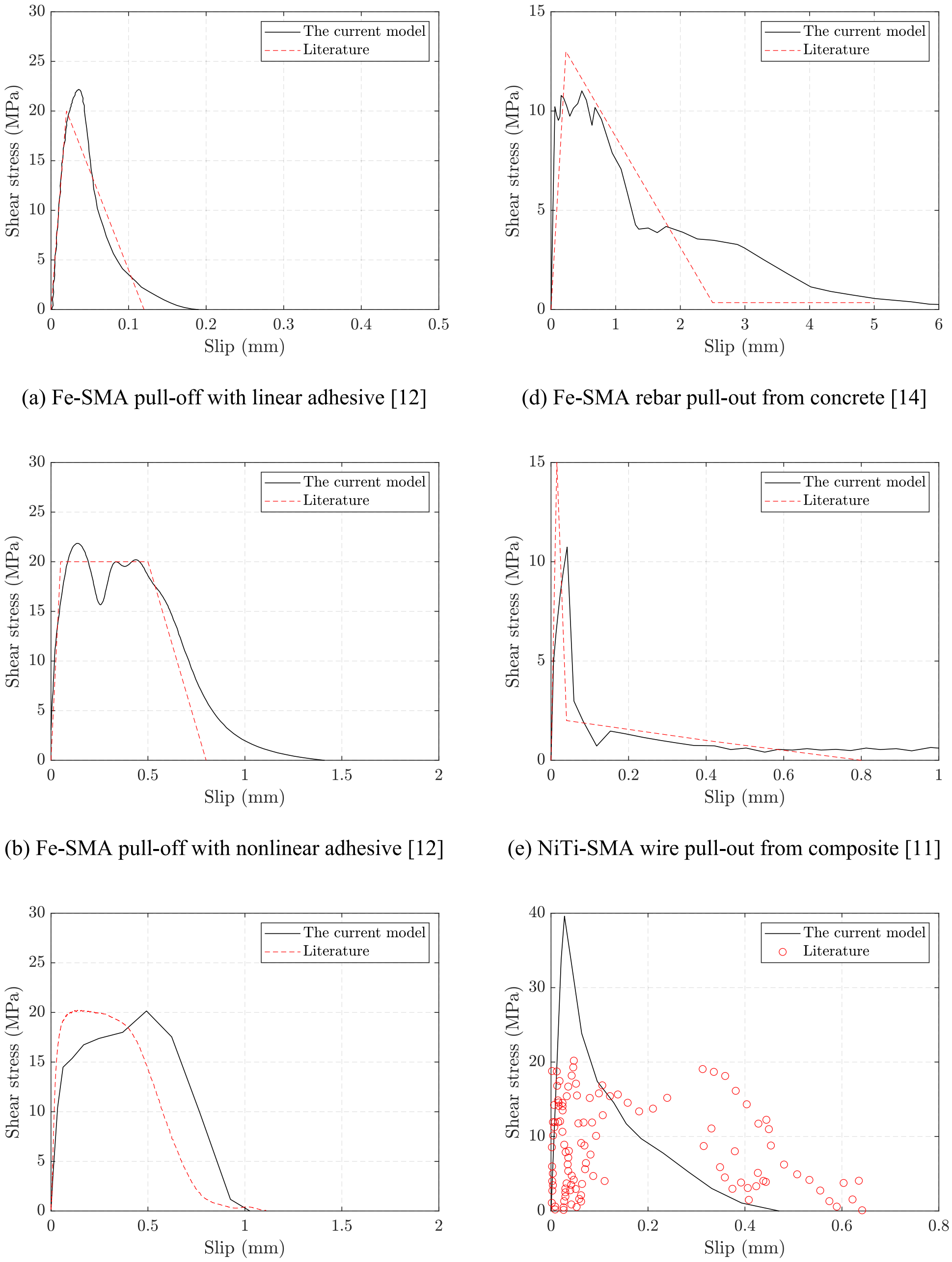

(a) Fe-SMA pull-off with linear adhesive [12]

(d) Fe-SMA rebar pull-out from concrete [14]

(b) Fe-SMA pull-off with nonlinear adhesive [12]

(e) NiTi-SMA wire pull-out from composite [11]

(c) CFRP strip pull-off with nonlinear adhesive [33]

(f) Steel rebar pull-out from concrete [36]

Fig. 13. Bond-slip behavior analyzed using the proposed post-processing method. The scales for shear stress and slip are adopted to best present the bond-slip curves, rather than facilitate a direct comparison among subfigures.

$$\tau = \frac{F}{b^2 \cdot t \cdot E} \cdot \frac{dF}{ds} \tag{20}$$

5. Discussion

5.1. Advantages of the proposed model

An advantage of the current model resides in the sufficient bond length, which allows for the fully dissipated interfacial fracture energy, validating Equation (10). The focus is exclusively on the very loaded end, i.e., the original bonding front. Examining intermediate states, such as deformations of adherents and adhesives, between the loaded end and free end, is not required.

A further advantage is the simultaneous determination of bond capacity and interfacial fracture energy, with minimal measurements, i.e., force-slip behavior at the loaded end. For bonded joints with adherents embedded, existing techniques typically use short bonds to characterize bond-slip behavior and long bonds to measure bond capacity. The current Wine Glass model integrates these two aspects, thus significantly simplifying the testing and analysis of bonding interface.

5.2. Limitations of the proposed model

Nevertheless, if the bond length is shorter than an effective bond length, Equation (10) is no longer valid, as the total interfacial fracture energy cannot be fully dissipated. Analyses should then rely on Equation (9), using partial fracture energy. Associating varying bond length, adherent nonlinear stress–strain behavior, and partial fracture energy analytically is challenging. Further development of the Wine Glass model is required.

Moreover, the current model works only on pure mode-II behavior, where the opening stress in the bonding interface is null or negligible. Interested readers are referred to Ref. [41] for mixed-mode I/II debonding behavior involving material and geometric nonlinearities.

5.3. Bonded joints comprising multi-layer interfaces

In a bonding system comprising a multi-layer interface, each layer should be analyzed, as fracture can occur in any layer. For example, a CFRP strip bonded onto a concrete block by adhesive, the thin adhesive layer is the first bonding interface, and the outermost layer of concrete is the second bonding interface. The Wine Glass model can be used to analyze the bond capacity in each layer, identifying the weakest layer with the smallest bond capacity for design. Further investigation with proper experimental design is needed to validate this design methodology.

6. Conclusions

This study investigates the bond capacity and bond-slip behavior of pull-off (lap-shear) and pull-out joints, by proposing an innovative Wine Glass model. This Wine Glass model offers an elegant graphical and analytical solution to the bond capacity, and its derivative provides an intuitive bond-slip post-processing method. The challenges arising from the adherent nonlinear stress–strain behavior are successfully addressed.

The bond capacity analysis using the Wine Glass model contains the following steps: (i) the adherent stress–strain curve plotted against stress-axis is regarded as a wine glass; (ii) the bonding fracture energy divided by the adherent strip thickness is regarded as the volume of wine in the wine glass; (iii) the wine level height corresponds to the adherent tensile stress at the bond capacity. The accuracy and robustness of the Wine Glass model have been validated on 95 pull-off (lap-shear) and pull-out tests involving linear and nonlinear adherents, linear and nonlinear adhesives, and various substrates materials.

In the bond-slip analysis, the shear stress is determined by multiplying the slope of the load-slip curve with the adherent tensile strain, while the slip is experimentally measured. The essential measurements for analyzing the bond-slip behavior are the joint load-slip behavior and adherent stress–strain behavior; both are commonly measured in experimental investigations.

The proposed Wine Glass model not only unveils the mechanism governing bond capacity but also provides a simple and robust method for bond-slip post-processing. Future research can be built upon this model to enhance the design and application of structures with bonding interfaces, such as new composite structures and the bonded strengthening of existing structures.

CRediT authorship contribution statement

Lingzhen Li: Writing – original draft, Methodology, Investigation, Formal analysis, Conceptualization. **Eleni Chatzi:** Writing – review & editing, Supervision, Formal analysis. **Christoph Czaderski:** Writing – review & editing. **Elyas Ghafoori:** Writing – review & editing, Supervision. **Xiao-Ling Zhao:** Funding acquisition, Project administration, Writing – review & editing, Supervision.

Declaration of competing interest

The authors declare that they have no known competing financial interests or personal relationships that could have appeared to influence the work reported in this paper.

Acknowledgements

The first author is sponsored by the Innovation and Technology Fund (ITF) Research Talent Hub of Hong Kong. A part of the work was done at the end of the PhD study of the first author at Empa and ETH Zurich, Switzerland. All authors would like to express their sincere gratitude to Prof. Dilum Fernando from The University of Edinburgh for his invaluable suggestions in improving this paper.

Appendix A. . Summary of experimental data vs. Wine Glass model prediction

Table 4 details the 95 pull-out/off joints used to validate the Wine Glass model. The joint types are: "EB" for external bonding (pull-off), "NSM" for near surface mounting (pull-out), and "Embedded" for rebar/wire embedded in substrate (pull-out). Due to the space limitation, only E-moduli of adherent materials are provided. For full stress–strain behaviors of nonlinear adherents, please refer to corresponding references. Specimen Symbols are adopted from literature.

Table 4
Details of pull-out/off joints.

Sp. No.	Sp. Symbol	Joint type	Adherent	Substrate	D(mm)	b(mm)	t(mm)	E(MPa)	G_f(MPa · mm)	$F_{b,test}$(kN)	$F_{b,pre}$(kN)	$\frac{F_{b,pre}}{F_{b,test}}$	Ref.
1	No. 3.	EB	CFRP strip	Concrete	–	60	2.4	165,000	0.39	31.10	33.15	1.07	[21]
2	1C-1	EB	CFRP strip	Concrete	–	50	0.111	240,000	0.65	9.90	9.30	0.94	[35]
3	2C-2	EB	CFRP strip	Concrete	–	50	0.222	240,000	0.71	13.40	12.90	0.96	
4	N150-1	NSM	CFRP strip	Concrete	–	16	3.6	160,000	2.08	44.13	35.03	0.79	[37]
5	N200-1	NSM	CFRP strip	Concrete	–	16	3.6	160,000	2.20	45.11	36.00	0.80	
6	N300-1	NSM	CFRP strip	Concrete	–	16	3.6	160,000	3.92	62.76	48.05	0.77	
7	CFRP-S1-T0.5-1	EB	CFRP strip	Steel	–	50	1.4	156,000	1.13	34.30	35.08	1.02	[34]
8	CFRP-S1-T0.5-2	EB	CFRP strip	Steel	–	50	1.4	156,000	1.13	35.90	35.08	0.98	
9	CFRP-A-T0.5-1	EB	CFRP strip	Steel	–	50	1.4	156,000	14.03	130.30	123.28	0.95	
10	CFRP-A-T0.5-2	EB	CFRP strip	Steel	–	50	1.4	156,000	14.03	110.30	123.28	1.12	
11	CFRP-S2-T0.5-1	EB	CFRP strip	Steel	–	50	1.4	156,000	12.84	124.40	119.16	0.96	
12	CFRP-S2-T0.5-2	EB	CFRP strip	Steel	–	50	1.4	156,000	12.84	134.80	119.16	0.88	
13	A-NM-T1-I	EB	CFRP strip	Steel	–	50	1.2	150,000	1.06	30.75	30.51	0.99	[19]
14	A-NM-T1-II	EB	CFRP strip	Steel	–	50	1.2	150,000	1.11	31.21	31.63	1.01	
15	C-NM-T1-I	EB	CFRP strip	Steel	–	50	1.2	150,000	12.34	112.87	106.00	0.94	
16	C-NM-T1-II	EB	CFRP strip	Steel	–	50	1.2	150,000	12.78	113.81	107.15	0.94	
17	A-NM-T1.5	EB	CFRP strip	Steel	–	50	1.2	150,000	1.27	35.20	33.77	0.96	
18	A-NM-T2	EB	CFRP strip	Steel	–	50	1.2	150,000	1.54	40.00	37.25	0.93	
19	A-NM-T3	EB	CFRP strip	Steel	–	50	1.2	150,000	1.11	33.80	31.63	0.94	
20	A-MM-T1	EB	CFRP strip	Steel	–	50	1.4	235,000	1.06	46.90	41.73	0.89	
21	A-HM-T1	EB	CFRP strip	Steel	–	50	1.4	340,000	1.31	63.80	55.93	0.88	
22	C-MM-T1	EB	CFRP strip	Steel	–	50	1.4	235,000	12.52	130.50	143.87	1.10	

Sp. No. | Sp. Symbol | Joint type | Adherent | Substrate | D(mm) | b(mm) | t(mm) | E(MPa) | G_f(MPa · mm) | $F_{b,test}$(kN) | $F_{b,pre}$(kN) | $\frac{F_{b,pre}}{F_{b,test}}$ | Ref.

(continued on next page)

Table 4 (*continued*)

Sp. No.	Sp. Symbol	Joint type	Adherent	Substrate	D(mm)	b(mm)	t(mm)	E(MPa)	G_f(MPa · mm)	$F_{b,test}$(kN)	$F_{b,pre}$(kN)	$\frac{F_{b,pre}}{F_{b,test}}$	Ref.
23	2-auto-400-w	Embedded	Fe-SMA rebar	Concrete	12	–	–	166,000	19.52	83.65	84.10	1.01	[14]
24	4-man-800-w	Embedded	Fe-SMA rebar	Concrete	12	–	–	166,000	24.31	80.12	77.23	0.96	
25	102–1	Embedded	NiTi-SMA wire	CFRP	0.77	–	–	45,770	0.88	0.32	0.28	0.90	[11]
26	102–2	Embedded	NiTi-SMA wire	CFRP	0.77	–	–	45,770	1.16	0.34	0.32	0.95	
27	Sika-1	EB	Fe-SMA strip	Steel	–	50	1.5	160,000	14.86	56.78	57.46	1.01	[20]
28	Sika-2	EB	Fe-SMA strip	Steel	–	50	1.5	160,000	14.86	56.52	57.46	1.02	
29	3 M−1	EB	Fe-SMA strip	Steel	–	50	1.5	160,000	6.87	54.61	52.07	0.95	
30	3 M−2	EB	Fe-SMA strip	Steel	–	50	1.5	160,000	6.87	52.96	52.07	0.98	
31	EA-1	EB	Fe-SMA strip	Steel	–	50	1.5	160,000	6.39	51.19	51.60	1.01	
32	EA-2	EB	Fe-SMA strip	Steel	–	50	1.5	160,000	6.39	49.71	51.60	1.04	
33	SS-EBR-L240	EB	Stainless steel strip	Concrete	–	20	5	192,000	0.35	15.90	16.34	1.03	[36]
34	SS-EBR-L300	EB	Stainless steel strip	Concrete	–	20	5	192,000	0.64	21.90	22.23	1.02	
35	SS-EBR-L400	EB	Stainless steel strip	Concrete	–	20	5	192,000	0.48	18.60	19.14	1.03	
36	SS-EBR-L560	EB	Stainless steel strip	Concrete	–	20	5	192,000	0.29	14.60	14.82	1.02	
37	SS-EBR-L640	EB	Stainless steel strip	Concrete	–	20	5	192,000	0.39	18.50	17.28	0.93	
38	SS-EBR-L800	EB	Stainless steel strip	Concrete	–	20	5	192,000	0.30	14.80	15.19	1.03	
39	SS-NSM-L200	Embedded	Stainless steel rebar	Concrete	8	–	–	195,000	5.23	48.90	50.82	1.04	
40	SS-NSM-L300	Embedded	Stainless steel rebar	Concrete	8	–	–	195,000	4.27	47.80	45.97	0.96	
41	C-1–150	EB	Fe-SMA strip	Steel	–	40	1.8	166,000	1.24	33.59	34.83	1.04	[31]
42	S-1–150	EB	Fe-SMA strip	Steel	–	40	1.8	166,000	1.56	38.27	37.33	0.98	
43	X-1–150	EB	Fe-SMA strip	Steel	–	40	1.8	166,000	1.69	39.80	38.13	0.96	
44	C-2–150	EB	Fe-SMA strip	Steel	–	40	1.8	166,000	1.04	32.33	32.71	1.01	
45	S-2–150	EB	Fe-SMA strip	Steel	–	40	1.8	166,000	1.44	38.12	36.52	0.96	
46	X-2–150	EB	Fe-SMA strip	Steel	–	40	1.8	166,000	1.70	38.44	38.16	0.99	
Sp. No.	Sp. Symbol	Joint type	Adherent	Substrate	D(mm)	b(mm)	t(mm)	E(MPa)	G_f(MPa · mm)	$F_{b,test}$(kN)	$F_{b,pre}$(kN)	$\frac{F_{b,pre}}{F_{b,test}}$	Ref.
47	A-0.5-200	EB	Fe-SMA strip	Steel	–	50	1.8	166,000	0.66	27.08	33.37	1.23	[30]
48	A-1.0–200	EB	Fe-SMA strip	Steel	–	50	1.8	166,000	0.95	31.99	39.18	1.22	
49	A-1.5-200	EB	Fe-SMA strip	Steel	–	50	1.8	166,000	0.94	32.28	38.83	1.20	
50	A-2.0–200	EB	Fe-SMA strip	Steel	–	50	1.8	166,000	0.93	31.19	38.89	1.25	
51	S-0.5-200	EB	Fe-SMA strip	Steel	–	50	1.8	166,000	1.20	36.15	42.95	1.19	
52	S-1.0–200	EB	Fe-SMA strip	Steel	–	50	1.8	166,000	1.49	40.19	45.85	1.14	
53	S-1.5-200	EB	Fe-SMA strip	Steel	–	50	1.8	166,000	1.70	40.72	47.72	1.17	

(*continued on next page*)

Table 4 (*continued*)

Sp. No.	Sp. Symbol	Joint type	Adherent	Substrate	D(mm)	b(mm)	t(mm)	E(MPa)	G_f(MPa · mm)	$F_{b,test}$(kN)	$F_{b,pre}$(kN)	$\frac{F_{b,pre}}{F_{b,test}}$	Ref.
54	S-2.0–200	EB	Fe-SMA strip	Steel	–	50	1.8	166,000	1.60	39.23	46.99	1.20	
55	L-0.5-200	EB	Fe-SMA strip	Steel	–	50	1.8	166,000	1.97	45.13	47.08	1.04	
56	L-1.0–200	EB	Fe-SMA strip	Steel	–	50	1.8	166,000	2.30	45.96	51.22	1.11	
57	L-1.5-200	EB	Fe-SMA strip	Steel	–	50	1.8	166,000	2.27	46.12	51.11	1.11	
58	L-2.0–200	EB	Fe-SMA strip	Steel	–	50	1.8	166,000	2.22	45.29	50.88	1.12	
59	S300-N-2/0	EB	Fe-SMA strip	Concrete	–	50	3	143,000	0.38	26.41	23.40	0.89	[32]
60	S350-N-2/0	EB	Fe-SMA strip	Concrete	–	50	3	143,000	0.38	27.16	23.40	0.86	
61	S400-N-2/0	EB	Fe-SMA strip	Concrete	–	50	3	143,000	0.38	27.98	23.40	0.84	
62	S300–200–2/0	EB	Fe-SMA strip	Concrete	–	50	3	143,000	0.49	27.50	26.85	0.98	
63	S350–200–2/0	EB	Fe-SMA strip	Concrete	–	50	3	143,000	0.49	33.12	26.85	0.81	
64	S400–200–2/0	EB	Fe-SMA strip	Concrete	–	50	3	143,000	0.49	30.52	26.85	0.88	
65	S300–300–2/0	EB	Fe-SMA strip	Concrete	–	50	3	143,000	0.29	17.47	20.55	1.18	
66	S350–300–2/0	EB	Fe-SMA strip	Concrete	–	50	3	143,000	0.29	22.58	20.55	0.91	
67	S400–300–2/0	EB	Fe-SMA strip	Concrete	–	50	3	143,000	0.29	18.89	20.55	1.09	
68	NS-S1-T0.5-1	EB	Fe-SMA strip	Steel	–	50	1.5	153,300	1.69	38.87	40.41	1.04	[12]
69	NS-S1-T0.5-2	EB	Fe-SMA strip	Steel	–	50	1.5	153,300	1.80	38.98	41.13	1.06	
70	NS-A-T0.5-1	EB	Fe-SMA strip	Steel	–	50	1.5	153,300	12.03	55.87	55.98	1.00	
71	NS-A-T0.5-2	EB	Fe-SMA strip	Steel	–	50	1.5	153,300	13.68	56.21	56.96	1.01	
72	NS-S2-T0.5-1	EB	Fe-SMA strip	Steel	–	50	1.5	153,300	15.22	59.09	57.81	0.98	
Sp. No.	Sp. Symbol	Joint type	Adherent	Substrate	D(mm)	b(mm)	t(mm)	E(MPa)	G_f(MPa · mm)	$F_{b,test}$(kN)	$F_{b,pre}$(kN)	$\frac{F_{b,pre}}{F_{b,test}}$	Ref.
73	NS-S2-T0.5-2	EB	Fe-SMA strip	Steel	–	50	1.5	153,300	17.44	58.93	58.84	1.00	[12]
74	PS-S1-T0.5-1	EB	Fe-SMA strip	Steel	–	50	1.5	137,500	1.28	33.55	33.68	1.00	
75	PS-S1-T0.5-2	EB	Fe-SMA strip	Steel	–	50	1.5	137,500	1.35	35.37	34.60	0.98	
76	PS-S1-T1-1	EB	Fe-SMA strip	Steel	–	50	1.5	137,500	1.31	34.66	34.07	0.98	
77	PS-S1-T1-2	EB	Fe-SMA strip	Steel	–	50	1.5	137,500	1.50	35.54	35.97	1.01	
78	PS-S1-T2-1	EB	Fe-SMA strip	Steel	–	50	1.5	137,500	1.45	36.69	35.35	0.96	
79	PS-S1-T2-2	EB	Fe-SMA strip	Steel	–	50	1.5	137,500	1.51	37.95	36.03	0.95	
80	PS-A-T0.5-1	EB	Fe-SMA strip	Steel	–	50	1.5	137,500	11.25	59.99	60.48	1.01	
81	PS-A-T0.5-2	EB	Fe-SMA strip	Steel	–	50	1.5	137,500	10.99	59.54	60.11	1.01	
82	PS-A-T1-1	EB	Fe-SMA strip	Steel	–	50	1.5	137,500	14.79	62.13	62.35	1.00	
83	PS-A-T1-2	EB	Fe-SMA strip	Steel	–	50	1.5	137,500	8.99	60.55	58.57	0.97	
84	PS-A-T2-1	EB	Fe-SMA strip	Steel	–	50	1.5	137,500	9.18	60.32	58.81	0.97	
85	PS-A-T2-2	EB	Fe-SMA strip	Steel	–	50	1.5	137,500	13.22	63.05	61.72	0.98	

(continued on next page)

Table 4 (*continued*)

Sp. No.	Sp. Symbol	Joint type	Adherent	Substrate	D(mm)	b(mm)	t(mm)	E(MPa)	G_f(MPa · mm)	$F_{b,test}$(kN)	$F_{b,pre}$(kN)	$\frac{F_{b,pre}}{F_{b,test}}$	Ref.
86	PS-S2-T0.5-1	EB	Fe-SMA strip	Steel	–	50	1.5	137,500	14.54	61.77	62.29	1.01	
87	PS-S2-T0.5-2	EB	Fe-SMA strip	Steel	–	50	1.5	137,500	15.69	62.33	62.94	1.01	
88	PS-S2-T1-1	EB	Fe-SMA strip	Steel	–	50	1.5	137,500	22.53	64.49	65.96	1.02	
89	PS-S2-T1-2	EB	Fe-SMA strip	Steel	–	50	1.5	137,500	20.28	65.27	64.97	1.00	
90	PS-S2-T2-1	EB	Fe-SMA strip	Steel	–	50	1.5	137,500	24.31	63.14	66.64	1.06	
91	PS-S2-T2-2	EB	Fe-SMA strip	Steel	–	50	1.5	137,500	24.31	66.79	66.64	1.00	
92	NS-S3-T0.5-1	EB	Fe-SMA strip	Steel	–	50	1.5	153,300	11.07	53.33	55.33	1.04	[13]
93	PS-S3-T0.5-1	EB	Fe-SMA strip	Steel	–	50	1.5	137,500	12.25	59.09	60.85	1.03	
94	N/A	EB	Mild steel strip	Steel	–	50	1.5	200,000	1.20	33.00	30.80	0.93	[33]
95	N/A	EB	Mild steel strip	Steel	–	50	1.5	200,000	12.50	36.00	33.75	0.94	

Data availability

Data will be made available on request.

References

[1] Cruz JR, Seręga S, Sena-Cruz J, Pereira E, Kwiecień A, Zając B. Flexural behaviour of NSM CFRP laminate strip systems in concrete using stiff and flexible adhesives. Compos B Engng 2020;195:108042. https://doi.org/10.1016/j.compositesb.2020.108042.
[2] Zheng B, Dawood M. Fatigue strengthening of metallic structures with a thermally activated shape memory alloy fiber-reinforced polymer patch. J Compos Constr 2017;21:04016113. https://doi.org/10.1061/(ASCE)CC.1943-5614.0000776.
[3] Aram MR, Czaderski C, Motavalli M. Debonding failure modes of flexural FRP-strengthened RC beams. Compos B Engng 2008;39:826–41. https://doi.org/10.1016/j.compositesb.2007.10.006.
[4] El-Hacha R, Chen D. Behaviour of hybrid FRP–UHPC beams subjected to static flexural loading. Compos B Engng 2012;43:582–93. https://doi.org/10.1016/j.compositesb.2011.07.004.
[5] Xia SH, Teng J. Behaviour of FRP-to-steel bonded joints. In: Proceedings of the International Symposium on Bond Behaviour of FRP in Structures, BBFS 2005, International Institute for FRP in Construction (IIFC); 2005. p. 411–8.
[6] Dai J, Ueda T, Sato Y. Development of the nonlinear bond stress–slip model of fiber reinforced plastics sheet–concrete interfaces with a simple method. J Compos Constr 2005;9:52–62. https://doi.org/10.1061/(ASCE)1090-0268(2005)9:1(52).
[7] Biolzi L, Ghittoni C, Fedele R, Rosati G. Experimental and theoretical issues in FRP-concrete bonding. Constr Build Mater 2013;41:182–90. https://doi.org/10.1016/j.conbuildmat.2012.11.082.
[8] Fernando D, Yu T, Teng JG. Behavior of CFRP laminates bonded to a steel substrate using a ductile adhesive. J Compos Constr 2014;18:04013040. https://doi.org/10.1061/(ASCE)CC.1943-5614.0000439.
[9] Jiang C, Yu Q-Q, Gu X-L. A unified bond-slip model for the interface between FRP and steel. Compos B Engng 2021;227:109380. https://doi.org/10.1016/j.compositesb.2021.109380.
[10] Calabrese AS, Colombi P, D'Antino T. Analytical solution of the full-range behavior of adhesively bonded FRP-steel joints made with toughened adhesives. Engng Fract Mech 2023;292:109569. https://doi.org/10.1016/j.engfracmech.2023.109569.
[11] El-Tahan M, Dawood M. Bond behavior of NiTiNb SMA wires embedded in CFRP composites. Polym Compos 2018;39:3780–91. https://doi.org/10.1002/pc.24408.
[12] Li L, Wang W, Chatzi E, Ghafoori E. Experimental investigation on debonding behavior of Fe-SMA-to-steel joints. Constr Build Mater 2023;364:129857. https://doi.org/10.1016/j.conbuildmat.2022.129857.
[13] Li L, Chatzi E, Ghafoori E. Debonding model for nonlinear Fe-SMA strips bonded with nonlinear adhesives. Engng Fract Mech 2023;282:109201. https://doi.org/10.1016/j.engfracmech.2023.109201.
[14] Schranz B, Czaderski C, Vogel T, Shahverdi M. Bond investigations of prestressed, near-surface-mounted, ribbed memory-steel bars with full bond length. Mater Des 2020;196:109145. https://doi.org/10.1016/j.matdes.2020.109145.
[15] ASTM C. Standard test method for comparing concretes on the basis of the bond developed with reinforcing steel 1991.
[16] ASTM D1002. Standard test method for apparent shear strength of single-lap-joint adhesively bonded metal specimens by tension loading (metal-to-metal). Annual Book of ASTM Standards 2010.
[17] Achillides Z, Pilakoutas K. Bond behavior of fiber reinforced polymer bars under direct pullout conditions. J Compos Constr 2004;8:173–81.
[18] Schranz B, Czaderski C, Vogel T, Shahverdi M. Bond behaviour of ribbed near-surface-mounted iron-based shape memory alloy bars with short bond lengths. Mater Des 2020;191:108647. https://doi.org/10.1016/j.matdes.2020.108647.
[19] Yu T, Fernando D, Teng JG, Zhao XL. Experimental study on CFRP-to-steel bonded interfaces. Compos B Engng 2012;43:2279–89. https://doi.org/10.1016/j.compositesb.2012.01.024.
[20] Wang W, Hosseini A, Ghafoori E. Experimental study on Fe-SMA-to-steel adhesively bonded interfaces using DIC. Engng Fract Mech 2021;244:107553. https://doi.org/10.1016/j.engfracmech.2021.107553.
[21] Czaderski C, Soudki K, Motavalli M. Front and side view image correlation measurements on FRP to concrete pull-off bond tests. J Compos Constr 2010;14:451–63. https://doi.org/10.1061/(ASCE)CC.1943-5614.0000106.

[22] Mata-Falcón J, Haefliger S, Lee M, Galkovski T, Gehri N. Combined application of distributed fibre optical and digital image correlation measurements to structural concrete experiments. Engng Struct 2020;225:111309. https://doi.org/10.1016/j.engstruct.2020.111309.

[23] Zhou J, Kang C, Peng M, Stümpel M, Marx S. Investigations on bond performances of GFRP/stainless steel reinforcements using distributed fiber optical sensors (DFOSs). J Build Eng 2023;75:106881.

[24] Aghabagloo M, Carreras L, Barahona M, Barris C, Baena M. Experimental study and numerical prediction of the bond-slip law for concrete elements strengthened with FRP using metaheuristic algorithm. Constr Build Mater 2024;411:134712.

[25] Szeptyński P. Analytical model of a composite girder with flexible adhesive bondline 2024. https://doi.org/10.24423/AOM.4498.

[26] Szeptyński P, Jasińska D, Mikulski L. Analytical modelling and shape optimization of composite girder with adhesive bondline. J Theor Appl Mech 2024: 129–42. https://doi.org/10.15632/jtam-pl/177259.

[27] Szeptyński P, Nowak M. Qualitative analysis of the influence of the non-linear material characteristics of flexible adhesive on the performance of lap joints. Compos Struct 2021;260:113539. https://doi.org/10.1016/j.compstruct.2020.113539.

[28] Li L, Chatzi E, Czaderski C, Zhao X-L, Ghafoori E. A Graphical Solution to Bond Capacity. Salerno, Italy: Assessment and Rehabilitation of Civil Structures; 2024.

[29] Pinterest. Schott Zwiesel Pure Tour Pinot Noir Glass 24-Oz. + Reviews | Crate & Barrel n.d. https://www.pinterest.com/pin/233413193176555708/.

[30] Wu Y, Qiang X, Jiang X, Meng X, Tang Y. Experimental study on bonding properties of Fe-SMA-to-steel bonded interface. Engng Struct 2024;306:117779. https://doi.org/10.1016/j.engstruct.2024.117779.

[31] Shu Y, Qiang X, Jiang X, Li Y. Experimental and theoretical study on mechanical performance of Fe-SMA/steel single lap joints. Thin-Walled Struct 2024;199: 111824. https://doi.org/10.1016/j.tws.2024.111824.

[32] Dong Z, Sun X, Sun Y, Zhu H, Wang H, Zhang P, et al. Experimental investigation on anchoring and bonding properties between Fe-SMA strip and concrete. Constr Build Mater 2024;438:137141. https://doi.org/10.1016/j.conbuildmat.2024.137141.

[33] Li L. Bond behavior and debonding failure in Fe-SMA strengthened steel members. ETH Zurich 2023. https://doi.org/10.3929/ETHZ-B-000637238.

[34] Li L, Pichler N, Chatzi E, Ghafoori E. Estimation of the mechanical behavior of CFRP-to-steel bonded joints with quantification of uncertainty. Engng Struct 2022;266:114573. https://doi.org/10.1016/j.engstruct.2022.114573.

[35] Zhu H, Wu G, Shi J, Liu C, He X. Digital image correlation measurement of the bond–slip relationship between fiber-reinforced polymer sheets and concrete substrate. J Reinf Plast Compos 2014;33:1590–603. https://doi.org/10.1177/0731684414541017.

[36] Biscaia H, Franco N, Chastre C. Stainless steel bonded to concrete: an experimental assessment using the DIC technique. Int J Concr Struct Mater 2018;12:9.

[37] Seo S-Y, Feo L, Hui D. Bond strength of near surface-mounted FRP plate for retrofit of concrete structures. Compos Struct 2013;95:719–27. https://doi.org/10.1016/j.compstruct.2012.08.038.

[38] Wang H-T, Wu G. Bond-slip models for CFRP plates externally bonded to steel substrates. Compos Struct 2018;184:1204–14. https://doi.org/10.1016/j.compstruct.2017.10.033.

[39] Li L, Martinelli E, Wang W, Chatzi E, Ghafoori E. Influence of post-processing methods on bond-slip behavior of nonlinear Fe-SMA lap-shear joints. Case Stud Constr Mater 2024;21:e03485. https://doi.org/10.1016/j.cscm.2024.e03485.

[40] Cladera A, Weber B, Leinenbach C, Czaderski C, Shahverdi M, Motavalli M. Iron-based shape memory alloys for civil engineering structures: an overview. Constr Build Mater 2014;63:281–93. https://doi.org/10.1016/j.conbuildmat.2014.04.032.

[41] Pichler N, Wang W, Li L, Ghafoori E, Motavalli M. Mixed-mode failure of adhesively bonded CFRP and iron-based shape memory alloy joints: experiments and modeling. Engng Struct 2025;326:119486. https://doi.org/10.1016/j.engstruct.2024.119486.